AIAA JOURNAL
Vol. 41, No. 9, September 2003

Computational Fluid Dynamics-Based Drag Prediction and Decomposition

Luigi Paparone*
Centro Italiano Ricerche Aerospaziali, 81043 Capua, Italy
and
Renato Tognaccini†
Università degli Studi di Napoli "Federico II," 80125 Naples, Italy

A method for the computation and breakdown of the aerodynamic drag into viscous and wave components is proposed. Given a numerical solution of the Reynolds averaged Navier–Stokes equations, the method, based on a Taylor's series expansion of the far-field drag expression, allows for the determination of the drag related to entropy variations in the flow. The identification of a spurious contribution, due to the numerical dissipation and discretization error of the flow solver algorithm, allows for drag computations weakly dependent on mesh size. Therefore, accurate drag evaluations are possible even on moderately sized grids. Results are presented for transonic flows around an airfoil and a wing–body configuration.

Nomenclature

a	=	local sound speed
b	=	wing span
C_D	=	drag coefficient, $D/(1/2\rho_\infty V_\infty^2 S_{\text{ref}})$
C_L	=	lift coefficient, $L/(1/2\rho_\infty V_\infty^2 S_{\text{ref}})$
C_p	=	pressure coefficient, $(p - p_\infty)/(1/2\rho_\infty V_\infty^2)$
c	=	airfoil chord
D	=	drag
$\boldsymbol{F}$	=	total force
H	=	total enthalpy
k	=	thermal conductivity
L	=	lift
M_∞	=	freestream Mach number
$\boldsymbol{n}$	=	unit vector normal to surface S
Pr	=	Prandtl number
p	=	static pressure
R	=	gas constant
Re_∞	=	freestream Reynolds number
S	=	surface of volume Ω
s	=	entropy
T	=	temperature
u, v, w	=	components of the velocity vector in $Oxyz$
$\boldsymbol{V}$	=	velocity vector
V_∞	=	freestream velocity
y^+	=	spatial coordinate in the direction normal to the wall in the law-of-the-wall coordinate
α	=	angle of attack
γ	=	specific heat ratio
μ_l	=	dynamic viscosity
μ_t	=	eddy viscosity
ρ	=	density
$\boldsymbol{\tau}$	=	viscous stress tensor
Φ	=	dissipation function
Ω	=	flow domain

Received 3 April 2001; revision received 16 October 2002; accepted for publication 13 March 2003.

*Senior Researcher, Dipartimento di Fluidodinamica; l.paparone@cira.it.
†Associate Professor, Dipartimento di Progettazione Aeronautica; renato.tognaccini@unina.it.

I. Introduction

WHEN the problem of drag computation from computational fluid dynamics calculations was addressed, Slooff[1] asked, "Mission impossible?" Despite the progress in this field, the question is still open today, and much research has been devoted to this subject. In addition to the dedicated conference where Ref. 1 was presented, it is possible to find a review with the fundamentals of physics in Ref. 2 and a more recent, extended, and detailed overview of the state of the art on drag prediction methods in Ref. 3.

The numerical computation of drag by surface integration of stresses (near-field method) usually gives insufficiently accurate results even if the flow solution is locally accurate (in terms of pressure and velocity profiles, for instance). In particular, for numerical solutions of the Euler/Reynolds averaged Navier–Stokes (RANS) equations, which are discussed in this work, the problem is mainly related to the presence of the numerical artificial dissipation and of the discretization error, which produces an artificial or spurious drag. This contribution becomes negligible only for unfeasible calculations with infinitely dense grids.

A second problem is that the near-field drag computation only allows for a distinction between pressure and friction drag. Additional useful information would be the breakdown into other physical components, such as viscous drag (associated with boundary layers), wave drag (associated with possible shock waves in transonic and supersonic flows), and lift-induced or vortex drag (associated with the free-vortex system shedding from three-dimensional lifting bodies). This task is relatively simple when drag has to be extracted by classical viscous–inviscid interaction methods. However, in the case of analysis performed by RANS methods such as in wind-tunnel experiments, the physical drag source is not isolated, and the breakdown into individual components becomes difficult. In practice, for a real flow there is not a clear definition of the different drag contributions.

In the present work, a solution to these problems is proposed when the drag associated with entropy production in a RANS solution is considered. This entropy drag is made up of viscous and wave components, and it represents the total drag for two-dimensional flows.

The proposed method is based on a far-field approach in which the drag is determined from the momentum integral balance by considering fluxes evaluated on a surface far from the body. In practice, far-field methods are the numerical techniques corresponding to the experimental drag determination obtained by measuring the momentum defect in the body wake.[4] This approach is equivalent, both theoretically and numerically, to the near-field method, but it allows for further development.

Oswatitsch[5] derived a far-field formula of the entropy drag considering first-order effects, in which the drag is expressed as the flux of a function only dependent on entropy variations. Lock[6] used Oswatitsch's formula for computing the wave drag in inviscid flows in terms of entropy jumps across the shocks. In Refs. 7 and 8, Oswatitsch's formula is used for computing the entropy drag in RANS solutions by limiting the far-field flux computation to a box enclosing the aircraft. However, this method does not eliminate the error due to the spurious drag, which is mostly concentrated near the configuration surface (where larger flow gradients and grid metric variations are present), and does not allow for the breakdown into constituent drag components. Indeed when fluxes are computed on surfaces far from the configuration, it is difficult to distinguish between wave and viscous contributions for streamlines crossing both the inviscid shock and the boundary layer. This is a major problem for the breakdown of drag by far-field methods as noted in Ref. 2.

In Ref. 9, a viscous and a wave drag contribution for a transonic airfoil flow has been computed by separately applying Oswatitsch's formula in the boundary layer wake and just aft the shock wave. Nevertheless, this method seems difficult to extend to the analysis of complex three-dimensional flows and, again, does not account for spurious drag contributions.

An interesting idea was exploited in Ref. 10 for inviscid Euler flows. Gauss's theorem allows for the replacement of the surface integral in Oswatitsch's formula with a volume integral; therefore, the integrand can be set to zero a priori in regions where it is known that physical entropy variations should be zero, thus, removing spurious contributions to drag.

In the following sections, a general far-field expression of drag is derived by Taylor's series expansion with respect to entropy, pressure, and total enthalpy variations. In this way, the entropy contribution can be separated from the drag due to lift. The first-order term is coincident with Oswatitsch's formula; it is shown, by numerical experiments, that for viscous flows this term is not sufficient for accurate drag prediction and that the additional second-order term is at least required.

The entropy drag is then expressed in terms of a volume integral that can be easily computed. In this way, it is possible to split drag into wave and viscous contributions once the shock wave and the boundary-layer/wake regions are properly identified. In addition, following Ref. 10, the spurious term associated with the volume integration in the remaining part of the flow can be eliminated, which allows for accurate drag predictions with medium-sized grids.

This method has been used to derive the lift vs drag curves of an airfoil. The results obtained in the case of transonic flow are presented and compared with experiments. In addition, the feasibility of the method to compute and split drag for complex flows is shown by presenting the breakdown of drag at different lifts obtained for a wing–body configuration in transonic flow conditions.

II. Aerodynamic drag

A steady fluid flow with free stream velocity V_∞ around an unpowered aircraft configuration is considered, implying that the only external force acting on the body is due to the fluid.

The integral momentum balance for a volume Ω surrounding the body allows for the following definitions of the aerodynamic force acting on the configuration:

$$\boldsymbol{F} = \int_{S_{\text{body}}} [(p - p_\infty)\boldsymbol{n} - (\boldsymbol{\tau}\cdot\boldsymbol{n})]\,\mathrm{d}S = -\int_{S_{\text{far}}} [\rho\boldsymbol{V}\boldsymbol{V} + (p - p_\infty)\boldsymbol{U} - \boldsymbol{\tau}]\cdot\boldsymbol{n}\,\mathrm{d}S \tag{1}$$

$\boldsymbol{U}$ is the unit tensor, and $\boldsymbol{n}$ is the unit normal vector pointing outside the volume Ω and normal to its surface, which is decomposed as $S_{\text{body}} \cup S_{\text{far}}$ with S_{body} specifying the aircraft surface and S_{far} the external surface bounding the volume Ω. In relation (1), nonslip or tangential flow on the body walls ($\boldsymbol{V}\cdot\boldsymbol{n} = 0$ on S_{body}) has been assumed, which is a correct hypothesis for an unpowered configuration. Equation (1) shows that the body force can be evaluated through two different integrations: 1) by performing an integral of the acting stresses on the body surface (near field) and 2) by calculating the second integral of relation (1), that is, by evaluating the net momentum flux across the surface S_{far} (far field).

With reference to a Cartesian system ($Oxyz$) with the x axis aligned to the freestream velocity vector, the total drag is defined as the projection of the force $\boldsymbol{F}$ on the x direction. The first integral of Eq. (1) gives the well-known expression of the near-field total drag.

In a similar way, the x component of the second integral of Eq. (1) provides the far-field drag expression. In the wake of the aircraft, the viscous stresses quickly decrease in magnitude because of the lack of a body wall sustaining significant viscous stresses; thus, if the surface S_{far} is chosen sufficiently far from the body (at least 1 or 2 wing chords), it is possible to neglect them in the far-field expression of drag,[2] which simplifies to

$$D_{\text{far}} = -\int_{S_{\text{far}}} [(p - p_\infty)n_x + \rho u(\boldsymbol{V}\cdot\boldsymbol{n})]\,\mathrm{d}S \tag{2}$$

where u is the x component of the velocity vector.

III. Entropy Drag in Two-Dimensional Flows

In a two-dimensional subsonic flow, the far-field drag expression can be further simplified by considering the surface S_{far} infinitely far from the configuration, S_∞, and analyzing the behavior of

$$\int_{S_\infty} (p - p_\infty)\boldsymbol{n}\,\mathrm{d}S$$

As $S_{\text{far}} \to S_\infty$, the pressure field (subsonic) is described by the asymptotic solution given by a dipole for a nonlifting flow or by an infinite vortex in lifting flows. In the first case, $\Delta p = p - p_\infty$ behaves as $1/r^2$ [$r = \sqrt{(x^2 + z^2)}$] and in the second case as $1/r$. Hence, the integration of Δp on S_∞ is definitely zero for a dipole only. For instance, in the case of an isolated vortex, it can be easily verified that

$$\int_{S_\infty} (p - p_\infty)n_z\,\mathrm{d}S$$

is different than zero and proportional to the circulation of the vortex generating the field. However, because of the symmetry of the pressure field with respect to the z axis,

$$\lim_{S_{\text{far}} \to S_\infty} \int_{S_{\text{far}}} (p - p_\infty)n_x\,\mathrm{d}S = 0 \tag{3}$$

for both cases (vortex or dipole). Therefore, in the case of a subsonic flow around a lifting airfoil, the far-field drag expression (2) reduces to

$$D_{\text{far}} = -\int_{S_\infty} \rho u(\boldsymbol{V}\cdot\boldsymbol{n})\,\mathrm{d}S \tag{4}$$

Express $u = V\cos\delta$ with $\delta = \arctan(w/u)$ and expand in Taylor's series δ; then Eq. (4) becomes

$$D_{\text{far}} = -\int_{S_\infty} \rho V(\boldsymbol{V}\cdot\boldsymbol{n})\,\mathrm{d}S \tag{5}$$

Furthermore, for a perfect gas, it is possible to express the module of the velocity in terms of variations of total enthalpy, ΔH, entropy, Δs, and static pressure, Δp (Ref. 2):

$$V/V_\infty = \sqrt{1 + 2\left(\Delta H/V_\infty^2\right) - 2/\left[(\gamma - 1)M_\infty^2\right]\left((\Delta p/p_\infty + 1)^{(\gamma-1)/\gamma}\exp\{(\Delta s/R)[(\gamma - 1)/\gamma]\} - 1\right)} = f\left(\Delta p/p_\infty, \Delta s/R, \Delta H/V_\infty^2\right) \tag{6}$$

where γ is the ratio between the specific heats of the fluid. Hence, the drag in a two-dimensional flow can be expressed as the flux of $f(\Delta p/p_\infty, \Delta s/R, \Delta H/V_\infty^2)$ across S_∞:

$$D_{\text{far}} = -V_\infty \int_{S_\infty} \rho f\left(\frac{\Delta p}{p_\infty}, \frac{\Delta s}{R}, \frac{\Delta H}{V_\infty^2}\right) \boldsymbol{V}\cdot\boldsymbol{n}\,\mathrm{d}S \tag{7}$$

Similar relations have been proposed by van der Vooren and Slooff[2] on the Trefftz plane in three-dimensional flows (boundary layer plus wave drag) and by Masson et al.[11] for two-dimensional inviscid flows.

Relation (6) can be expanded in Taylor's series obtaining

$$\begin{aligned} V/V_\infty = {} & 1 + f_{p1}(\Delta p/p_\infty) + f_{s1}(\Delta s/R) + f_{H1}\left(\Delta H/V_\infty^2\right) \\ & + f_{p2}(\Delta p/p_\infty)^2 + f_{s2}(\Delta s/R)^2 + f_{H2}\left(\Delta H/V_\infty^2\right)^2 \\ & + f_{ps2}(\Delta p/p_\infty)(\Delta s/R) + f_{pH2}(\Delta p/p_\infty)\left(\Delta H/V_\infty^2\right) \\ & + f_{sH2}(\Delta s/R)\left(\Delta H/V_\infty^2\right) \\ & + \mathcal{O}\left[(\Delta p/p_\infty)^3, (\Delta s/R)^3, \left(\Delta H/V_\infty^2\right)^3, \ldots\right] \end{aligned} \tag{8}$$

The coefficients of the series expansion depend on γ and M_∞; they are

$$f_{p1} = -\frac{1}{\gamma M_\infty^2}, \qquad f_{s1} = -\frac{1}{\gamma M_\infty^2}, \qquad f_{H1} = 1 \tag{9}$$

$$f_{p2} = -\frac{1+\gamma M_\infty^2}{2\gamma^2 M_\infty^4}, \qquad f_{s2} = -\frac{1+(\gamma-1)M_\infty^2}{2\gamma^2 M_\infty^4}$$

$$f_{H2} = -\frac{1}{2} \tag{10}$$

$$f_{ps2} = -\frac{1+(\gamma-1)M_\infty^2}{\gamma^2 M_\infty^4}, \qquad f_{pH2} = \frac{1}{\gamma M_\infty^2}$$

$$f_{sH2} = \frac{1}{\gamma M_\infty^2} \tag{11}$$

After substitution of the expression (8) into Eq. (7), the contributions of pressure, entropy, and total enthalpy are isolated. Moreover, all terms with $\Delta p/p_\infty$ vanish on S_∞. This is because the momentum flux can be written as $\rho\boldsymbol{V} = \rho_\infty \boldsymbol{V}_\infty + \Delta(\rho\boldsymbol{V})$; therefore, all terms with pressure in Eq. (7) can be decomposed in two integrals. The integral associated with $\rho_\infty \boldsymbol{V}_\infty$ is zero due to the symmetry of the pressure field with respect to z axis [relation (3)]. The integral associated with $\Delta(\rho\boldsymbol{V})$ is also zero because both $\Delta p \cdot n_x$ and $\Delta\rho V \cdot n_x$ tend to zero as $S_{\text{far}} \to S_\infty$ in both the wake of the boundary layer and in the inviscid region. Hence, the general far-field drag expression around a body in two-dimensional flows becomes

$$\begin{aligned} D_{\text{far}} = -V_\infty \Bigg\{ & \int_{S_\infty} \left[f_{s1}\frac{\Delta s}{R} + f_{s2}\left(\frac{\Delta s}{R}\right)^2 \right] \rho(\boldsymbol{V}\cdot\boldsymbol{n})\,\mathrm{d}S \\ & + \int_{S_\infty} \left[f_{H1}\frac{\Delta H}{V_\infty^2} + f_{H2}\left(\frac{\Delta H}{V_\infty^2}\right)^2 \right] \rho(\boldsymbol{V}\cdot\boldsymbol{n})\,\mathrm{d}S \\ & + \int_{S_\infty} \left[f_{sH2}\frac{\Delta s}{R}\frac{\Delta H}{V_\infty^2} \right] \rho(\boldsymbol{V}\cdot\boldsymbol{n})\,\mathrm{d}S \Bigg\} \\ & + \mathcal{O}\left[\left(\frac{\Delta s}{R}\right)^3, \left(\frac{\Delta H}{V_\infty^2}\right)^3, \ldots \right] \end{aligned} \tag{12}$$

The first integral, depending only on Δs, is the entropy drag. The term depending on ΔH is, in general, different than zero in a boundary layer with $Pr \neq 1$ and if energy is added to the flow, that is, in the case of powered configuration. If second-order terms are considered, an interference contribution (depending on $\Delta s \cdot \Delta H$) is present.

In the case of $Pr \approx 1$ and power-off conditions, all terms depending on ΔH are negligible and, for two-dimensional flows, the entropy drag represents the total drag, given by the sum of the profile drag (friction plus form) and by the wave drag (shock waves).

The first-order contribution of the entropy drag is equal to the well-known drag expression derived by Oswatitsch,[5] widely used especially in the computation of the wave drag in inviscid flows.

IV. Entropy Drag in Three-Dimensional Flows

In three-dimensional lifting flows, relation (3) does not hold: In the far wake of the wing, pressure variations are still significant, and both terms of Eq. (2) need to be considered. This relation, with $u = \hat{v}_x V$ (where $\hat{v}_x$ the x component of the unit vector specifying the direction of the velocity) can be written as

$$D_{\text{far}} = -\int_{S_{\text{far}}} \left[\rho V_\infty^2 \frac{1}{\gamma M_\infty^2}\frac{\Delta p}{p_\infty} n_x + V_\infty \hat{v}_x \frac{V}{V_\infty}\rho(\boldsymbol{V}\cdot\boldsymbol{n}) \right] \mathrm{d}S \tag{13}$$

Again, after substitution of the series expansion (8) into expression (13), the far field drag can be written as

$$\begin{aligned} D_{\text{far}} = {} & -V_\infty \int_{S_{\text{far}}} \hat{v}_x \left[f_{s1}\frac{\Delta s}{R} + f_{s2}\left(\frac{\Delta s}{R}\right)^2 \right] \rho(\boldsymbol{V}\cdot\boldsymbol{n})\,\mathrm{d}S \\ & - V_\infty \int_{S_{\text{far}}} \hat{v}_x \left[f_{H1}\frac{\Delta H}{V_\infty^2} + f_{H2}\left(\frac{\Delta H}{V_\infty^2}\right)^2 \right] \rho(\boldsymbol{V}\cdot\boldsymbol{n})\,\mathrm{d}S \\ & - V_\infty \int_{S_{\text{far}}} \hat{v}_x \left[1 + f_{p1}\frac{\Delta p}{p_\infty} + f_{p2}\left(\frac{\Delta p}{p_\infty}\right)^2 \right] \rho(\boldsymbol{V}\cdot\boldsymbol{n})\,\mathrm{d}S \\ & - \rho V_\infty^2 \frac{1}{\gamma M_\infty^2} \int_{S_{\text{far}}} \frac{\Delta p}{p_\infty} n_x\,\mathrm{d}S \\ & - V_\infty \int_{S_{\text{far}}} \hat{v}_x \left[f_{ps2}\frac{\Delta p}{p_\infty}\frac{\Delta s}{R} + f_{sH2}\frac{\Delta s}{R}\frac{\Delta H}{V_\infty^2} \right] \rho(\boldsymbol{V}\cdot\boldsymbol{n})\,\mathrm{d}S \\ & + \mathcal{O}\left[\left(\frac{\Delta s}{R}\right)^3, \left(\frac{\Delta H}{V_\infty^2}\right)^3, \left(\frac{\Delta p}{p_\infty}\right)^3 \ldots \right] \end{aligned} \tag{14}$$

In this relation, four terms can be recognized:

1) The first integral is related with the entropy rise $\Delta s/R$; it is here defined as the entropy drag around a three-dimensional unpowered aircraft configuration, due to the direct effects of boundary layers and shock waves.

2) The second integral depends on ΔH and is not only related with drag. For instance, as shown in Ref. 7, it is strictly connected with thrust in the case of power-on conditions.

3) The third and fourth integrals are related to the pressure variations and to the angle between the local velocity vector $\boldsymbol{V}$ and the freestream direction, $\hat{v}_x$, which is not negligible downstream in the wake of lifting bodies. This contribution, only present in three-dimensional flows (viscous and inviscid), is here defined as induced or vortex drag.

4) The fourth integral, containing crossed second-order terms, represents interference effects among the three basic contributions (entropy, total enthalpy, and vortex).

In Eq. (14), the surface S_{far} is arbitrary. The only limitation concerns a sufficient distance from the trailing edges of the body to neglect viscous stresses in Eq. (2). Therefore, a margin of uncertainty in the definition of the different contributions must be considered because, although the sum is constant, each contribution can vary depending on the integration surface S_{far}. In particular, vortex drag can be converted in entropy drag as the distance of the surface S_{far} from the body increases.[8] However, note that this problem is present in all definitions of vortex drag for real flows. Despite these

limitations, the free-vortex system is incredibly stable in practice; it vanishes after hundreds of wing spans. Thus, the use of a definition with an integration surface taken few wing spans from the configuration is still effective. In the case of numerical solutions, the numerical diffusion of the entropy in the wing wake must be also taken into account, which causes a further conversion of the vortex drag into entropy drag. However, van Dam et al.[12] proved, by numerical experiments, the possibility to calculate with sufficient accuracy the induced drag of an elliptic wing in an inviscid flow determined by an Euler flow solver.

Because $\hat{v}_x = 1 + O[(v^2 + w^2)/V_\infty]$ the entropy drag for three-dimensional flows reduces to

$$D_{\Delta s} = -V_\infty \int_{S_{\text{far}}} \left[f_{s1} \frac{\Delta s}{R} + f_{s2} \left(\frac{\Delta s}{R} \right)^2 \right] \rho (\boldsymbol{V} \cdot \boldsymbol{n}) \, \mathrm{d}S \tag{15}$$

which is exactly the same expression found for two-dimensional flows.

Finally, with

$$g(\Delta s/R) = -f_{s1}(\Delta s/R) - f_{s2}(\Delta s/R)^2 \tag{16}$$

Equation (15) can be expressed in divergence form by applying the Gauss's theorem to the vector field $\rho g \boldsymbol{V}$ in the finite flow domain Ω. Because on S_{body} $\boldsymbol{V} \cdot \boldsymbol{n} = 0$, the entropy drag expression becomes

$$D_{\Delta s} = V_\infty \int_\Omega \nabla \cdot (\rho g \boldsymbol{V}) \, \mathrm{d}\Omega \tag{17}$$

V. Breakdown of Entropy Drag

The integrand in Eq. (17) is connected with the entropy production rate per unit volume,

$$\rho \dot{s} = (1/T)[\Phi + \nabla \cdot (k \nabla T)] \tag{18}$$

where T and k are the temperature and the thermal conductivity of the fluid, respectively, and Φ is the dissipation function (dissipation rate of kinetic energy). The differential balance equation of the entropy $\rho \boldsymbol{V} \cdot \nabla s = \rho \dot{s}$ leads to

$$\nabla \cdot \left[\rho g \left(\frac{\Delta s}{R} \right) \boldsymbol{V} \right] = R \frac{\partial g}{\partial s} \rho \boldsymbol{V} \cdot \nabla s = R \frac{\partial g}{\partial s} \rho \dot{s} \tag{19}$$

This property makes the entropy drag relation (17) particularly interesting because it associates drag to its local production; the integrand of Eq. (17) can be defined as the local production rate of entropy drag. Hence, provided an unique definition of the viscous (boundary layer plus wake) and of the shock wave regions, the domain Ω can be decomposed as $\Omega = \Omega_v \cup \Omega_w \cup \Omega_{\text{sp}}$. Ω_v is the volume containing the boundary layer and the viscous wake, Ω_w contains the shock waves, and Ω_{sp} specifies the remaining part of the flowfield (Fig. 1).

By use of relation (17), the entropy drag can be expressed as the sum of three contributions:

$$D_{\Delta s} = D_v + D_w + D_{\text{sp}} \tag{20}$$

with

$$D_v = V_\infty \int_{\Omega_v} \nabla \cdot (\rho g \boldsymbol{V}) \, \mathrm{d}\Omega, \qquad D_w = V_\infty \int_{\Omega_w} \nabla \cdot (\rho g \boldsymbol{V}) \, \mathrm{d}\Omega$$

$$D_{\text{sp}} = V_\infty \int_{\Omega_{\text{sp}}} \nabla \cdot (\rho g \boldsymbol{V}) \, \mathrm{d}\Omega \tag{21}$$

These are the definitions of boundary layer or viscous drag D_v and wave drag D_w adopted in the present work. D_{sp} is, in general, not zero if evaluated by using a numerical solution. It is due to the spurious entropy production associated with the artificial dissipation (implicit or explicit) and with the discretization error of the numerical scheme; it represents a numerical error that can be computed and eliminated. D_v and D_w can also be affected by spurious contributions. Therefore, D_{sp} does not represent, in general, the total unphysical drag of the numerical computation.

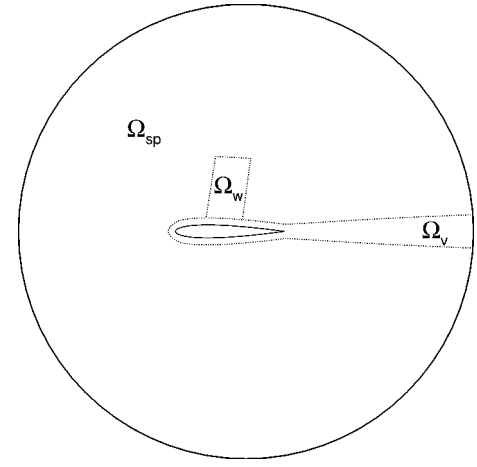

Fig. 1 Viscous shock wave and spurious entropy regions.

VI. Algorithms for Region Selection

It is clear that the proposed breakdown of entropy drag relies on a proper definition of the boundary-layer and shock wave region. For this purpose, a zone selection algorithm has been developed. Given a numerical RANS solution, the problem is to establish whether a grid cell, for which all thermofluidynamic information is known, belongs to the boundary layer, to the shock wave, or to the remaining part of the flow domain. Equation (17) in divergence form allows for a simple computation of the drag, as suggested in Ref. 10, by transforming the volume integral into the surface integral for each grid cell. Indeed, by specifying with N_v, N_w, and N_{sp} the number of grid cells belonging to the viscous region, the shock wave region, and the spurious region, respectively, the drag contributions equations (21) can be numerically computed as

$$D_v = \sum_{j=1}^{N_v} \int_{S_j} \boldsymbol{n} \cdot \rho g \boldsymbol{V} \, \mathrm{d}S_j, \qquad D_w = \sum_{j=1}^{N_w} \int_{S_j} \boldsymbol{n} \cdot \rho g \boldsymbol{V} \, \mathrm{d}S_j$$

$$D_{\text{sp}} = \sum_{j=1}^{N_{\text{sp}}} \int_{S_j} \boldsymbol{n} \cdot \rho g \boldsymbol{V} \, \mathrm{d}S_j \tag{22}$$

where S_j is the surface of the j-grid cell.

In the shock/boundary-layer interaction region, a distinction between viscous and shock wave cells becomes ambiguous. In the present method a hierarchy has been chosen in the selection criteria: First the shock wave region test is performed; if not satisfied, the viscous region test follows; if not satisfied, the cell is assumed belonging to the spurious region.

The algorithm required for the computations of the integrals in Eqs. (21) is particularly simple for both structured and unstructured numerical solutions. It does not require the computation of intersections of the flowfield with given planes. If required, the algorithm can be easily made consistent with the differential scheme used in the flow solver generating the flow solution.

A. Shock Wave Region

The automatic selection of the shock wave region relies on a sensor based on the following nondimensional function:

$$F_{\text{shock}} = (\boldsymbol{V} \cdot \nabla p)/(a|\nabla p|) \tag{23}$$

where a is the local sound speed. This sensor is negative in expansion zones (where obviously shock waves are not present) and positive in compression regions. Thus, cells with negative values of F_{shock} can be automatically excluded from the shock wave region.

A further selection can be made because this sensor provides a guess of the local Mach number component in the direction of the pressure gradient. $F_{\text{shock}} > 1$ in the compression zone implies that the corresponding cell is in the neighborhood (upwind) of a shock wave. Furthermore, it is also possible to get an estimation of the Mach number downstream of the shock when the Rankine–Hugoniot relations are used. This value can be used as a cutoff, K_{cw}, for the shock function and allows the selection of cells both upstream and downstream of the shock wave if the test $F_{\text{shock}} > K_{cw}$ is satisfied.

B. Boundary-Layer and Wake Region

The identification of a proper automatic sensor for the detection of the boundary layer and wake required greater effort. A first difficulty is given by the requirement of a topology-independent selection criteria to allow for an algorithm independent of the configuration and also applicable to unstructured data. Therefore, a sensor based on the boundary-layer thickness (which on the other hand is ambiguous and strongly dependent on a cutoff value) cannot be used. Furthermore, the sensors cannot be based on variables related to the entropy production, for instance, the dissipation of kinetic energy, because they tend to also detect the spurious region.

In the present work, a sensor properly working for turbulent flows is introduced. In this case, the eddy viscosity is a reliable measure of the relevance of the viscous effects. The adopted sensor is

$$F_{\text{bl}} = (\mu_l + \mu_t)/\mu_l \tag{24}$$

where μ_l and μ_t are the dynamic and eddy viscosities, respectively. The value of F_{bl} is very high in the boundary layer and wake, whereas it is ≈ 1 in the remaining part of the domain. The viscous region is selected by checking if $F_{\text{bl}} > K_{\text{bl}} \cdot F_{\text{bl}\infty}$, where $F_{\text{bl}\infty}$ is the freestream value of the boundary-layer sensor. K_{bl} is a cutoff value for the boundary-layer selection; in all present results, $K_{\text{bl}} = 1.1$ has been used. The interesting feature of the present selection criteria is that the drag breakdown did not appear to be sensitive to the input cutoff value.

VII. Results

The flow simulations, which are the basis for the drag analysis, have been obtained solving the steady Euler and RANS equations on block structured grids, by a standard technique based on the well-known central space discretization, with self-adaptive explicit second- and fourth-order artificial dissipation.[13] Two turbulence models have been used, the Baldwin–Lomax[14] for the two-dimensional test and the Spalart–Allmaras[15] for the wing–body test.

A. Two-Dimensional Airfoil, Inviscid Flow

The first test is the inviscid flow simulation around a NACA 0012 airfoil. The freestream conditions are $M_\infty = 0.8$ and $\alpha = 0$ deg. The mesh is a single block O-type grid with three grid levels made up of 64×32, 128×64, and 256×128 cells, respectively. In the following, the three grid levels are specified as coarse c, medium m, and fine f. The surface pressure distributions obtained on the three grids are shown in Fig. 2.

In the present case, the only drag contribution is given by the wave drag associated with the strong shock wave at $x/c \approx 0.5$. In Fig. 3, the near- and far-field C_D are plotted vs the mesh size, where $h = 1$ specifies the finest grid level. The near-field drag for the three grids is $C_{Dc} = 106$, $C_{Dm} = 86$, and $C_{Df} = 83$ drag counts (1 drag count $= 0.0001$). The far-field drag is practically coincident with the near-field C_D, except for a small difference on the coarse mesh (1 count). The strong variation of the C_D with the mesh size ($\approx 20\%$ variation between coarse and fine grid) is evident, due to the large spurious drag of the coarser solutions.

On the other hand, it is possible to compute C_{D_w} using the present wave drag definition (20), that is, limiting the computation of the integral to the shock region. An example of the region automatically selected for the integration is presented in Fig. 4 (coarse grid). The drag variation between coarse and fine grid reduces from 20 to 4% (Fig. 3). In practice, the spurious contribution is completely eliminated. A similar result has been obtained in Ref. 10 by applying

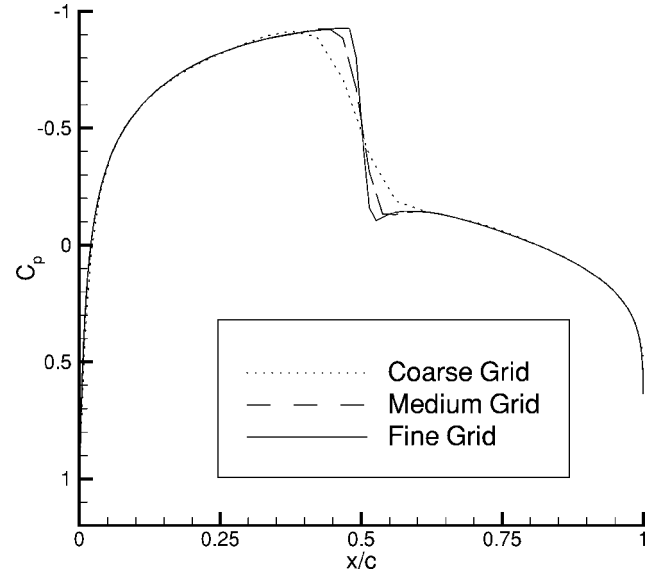

Fig. 2 NACA 0012, inviscid test: surface pressure distributions, $M_\infty = 0.8$, and $C_L = 0$.

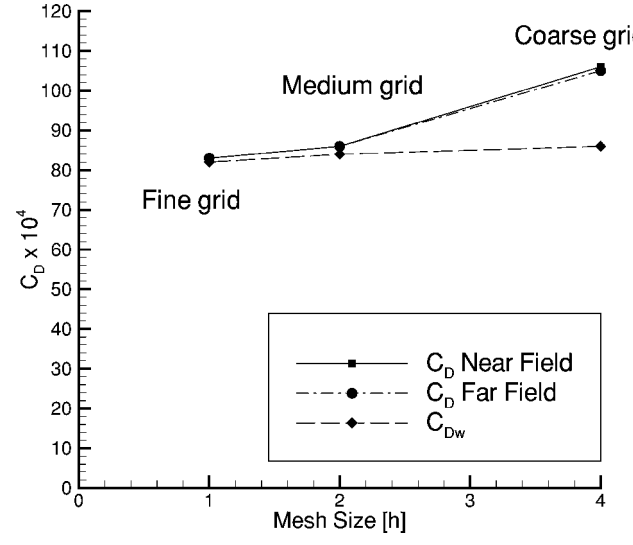

Fig. 3 NACA 0012, inviscid test: near- and far-field C_D vs mesh size, $M_\infty = 0.8$, and $C_L = 0$.

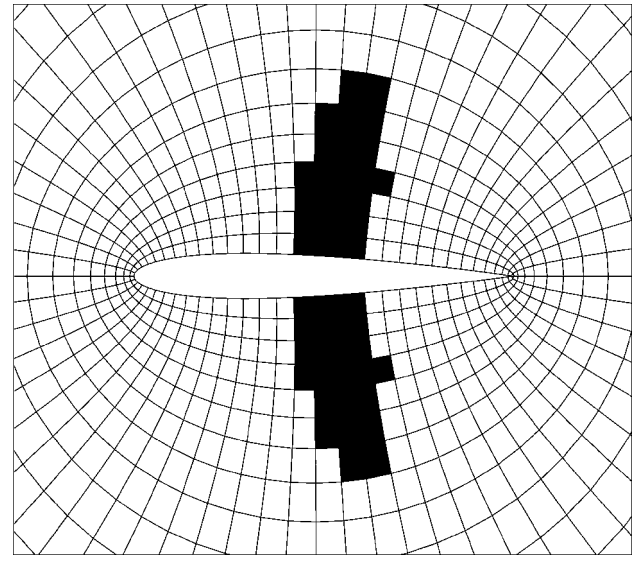

Fig. 4 NACA 0012, inviscid test: selected region for the wave drag computation, coarse grid, $M_\infty = 0.8$, and $C_L = 0$.

Oswatitsch's formula. This result suggests the feasibility to predict the wave drag accurately by present method, even on a coarse mesh.

B. Two-Dimensional Airfoil, Viscous Flow

The polar curve (C_L vs C_D) of the NACA 0012 airfoil has been computed at freestream conditions, $M_\infty = 0.7$ and $Re_\infty = 9 \times 10^6$. Present results have been compared with the experimental data set[16] that was proposed as reference in an AGARD workshop dedicated to drag prediction.[17] The mesh is a single-block C-type grid with four grid levels, made up of 80×32, 160×64, 320×128, and 640×256 cells. A measure of the grid resolution is given by the distance from the body wall of the first grid point expressed by the turbulent law of the wall coordinate y^+. For the fine grid, $y^+ \approx 1$, for the superfine grid (640×256 cells) $y^+ \approx 0.5$. The fine grid is sufficient for accurate engineering computations. The superfine grid has been used to check the convergence of the solution as mesh size $h \to 0$.

The surface pressure distributions on the medium, fine, and superfine grids are compared with the experiments at $C_L = 0.5$ in Fig. 5. The agreement is satisfactory both in terms of pressure peak and shock wave location. At lower C_L, the agreement is even better, suggesting that all of the main flow features have been adequately resolved for the analyzed flow conditions. For the $C_L = 0.6$ test, some discrepancy appears, indicating the limit of applicability of the Baldwin–Lomax turbulence model.

In Table 1, the viscous and wave drag computed by using Oswatitsch's formula, computed by Eq. (17) with second-order entropy terms, and computed by the exact formula (7) are compared for three different angles of attack with superfine grid and $M_\infty = 0.7$ and $Re_\infty = 9 \times 10^6$. The second-order approximation agrees with relation (7) for both viscous and wave drag. However, the first-order approximation underestimates viscous drag 3%. This result is caused by the entropy variations in the boundary layer that are larger (by order of magnitudes) than the variations across shock waves. Therefore, whereas a first-order approximation can be sufficient in the case of wave drag, a second-order term at least is required in the boundary layer. In the sequel, the far-field C_D is always computed by retaining the second-order approximation.

Table 1 NACA 0012, viscous test: comparison of $C_{D_v} \times 10^4$ and $C_{D_w} \times 10^4$

	$C_L = 0.000$		$C_L = 0.424$		$C_L = 0.666$	
Method	C_{D_v}	C_{D_w}	C_{D_v}	C_{D_w}	C_{D_v}	C_{D_w}
First-order formula	76.1	0.0	84.1	17.5	115.8	140.5
Second-order formula	78.6	0.0	86.8	17.5	118.4	140.5
Equation (7)	78.6	0.0	86.9	17.5	119.3	140.5

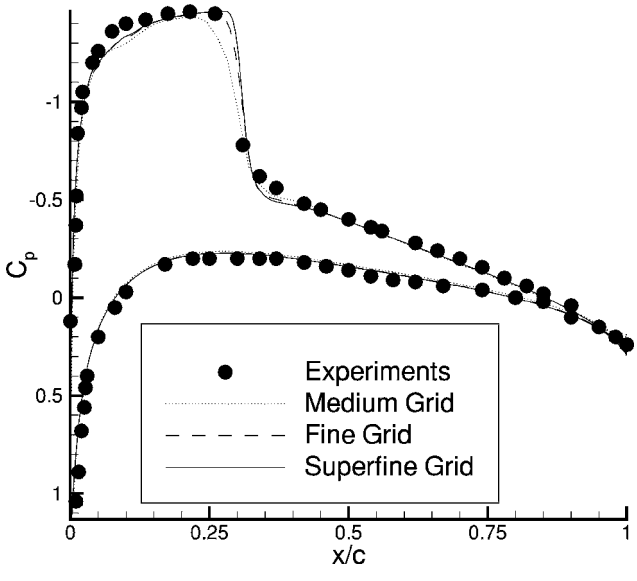

Fig. 5 NACA 0012, viscous test: surface pressure distributions, $M_\infty = 0.7$, $Re_\infty = 9 \times 10^6$, and $C_L = 0.5$.

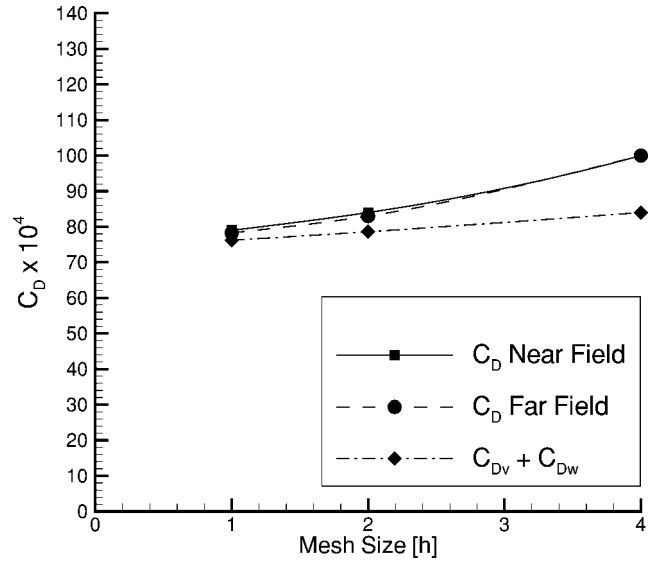

Fig. 6 NACA 0012, viscous test: far-field C_D vs mesh size, $M_\infty = 0.7$, $Re_\infty = 9 \times 10^6$, and $C_L = 0$.

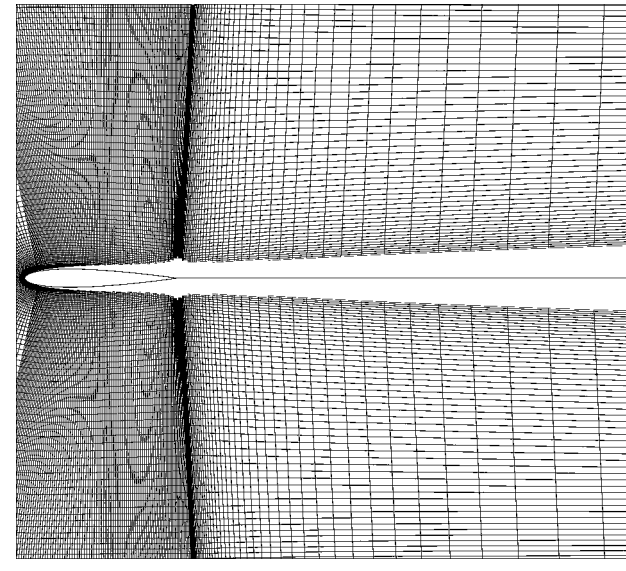

Fig. 7 NACA 0012, viscous test: viscous region selected in the fine-grid test, $M_\infty = 0.7$, $Re_\infty = 9 \times 10^6$, and $C_L = 0$.

Also in this case, the application of the breakdown algorithm allows for the identification of a spurious contribution that can be removed from the drag computation. As in the inviscid case, the drag variation with the mesh size is considerably reduced (Fig. 6, $C_L = 0$ case); indeed, the variation of the computed drag between the medium and the superfine grid is reduced from 22 to 9% by restricting the calculation of the integral (17) to the region visualized in Fig. 7. The sum $C_{D_v} + C_{D_w}$ on the coarser grids is still larger than the obtained value for the superfine grid, which suggests that the spurious drag has not been completely removed. On the coarse grid level, the spurious drag contribution is still present in the boundary-layer region. For all tests, the drag contribution of ΔH in Eq. (12) has also been computed. It has been verified that this term tends to zero as $h \to 0$ (less than 1 count on the superfine grid level).

The obtained results are confirmed for a lifting case (Fig. 8). In this test, the spurious drag $C_{D_{sp}}$ ranges from 20 counts ($h = 4$ grid) to 1 count ($h = 1$ grid) and $C_{D_v} + C_{D_w}$ only differs 7 counts among tests at $h = 4$ and 1. The viscous and shock wave regions selected are plotted in Fig. 9. The strange behavior of the selected wake, which is symmetrical even for this lifting case, is due to use of a symmetrical grid with the Baldwin–Lomax turbulence model. However, it has

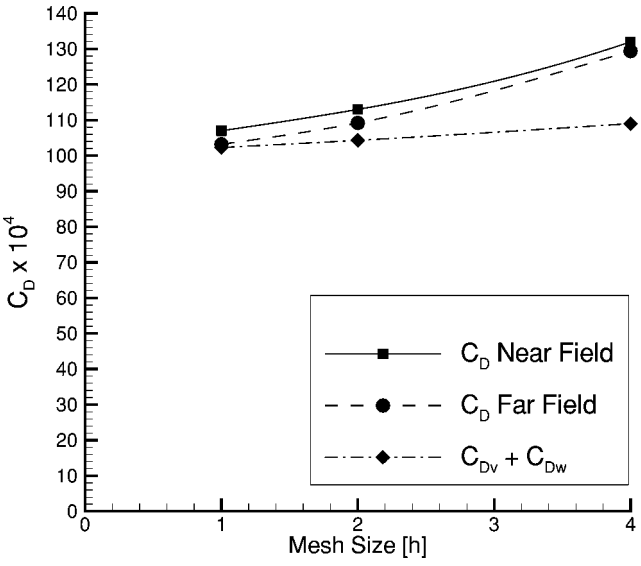

Fig. 8 NACA 0012, viscous test: far-field C_D vs mesh size, $M_\infty = 0.7$, $Re_\infty = 9 \times 10^6$, and $C_L = 0.424$.

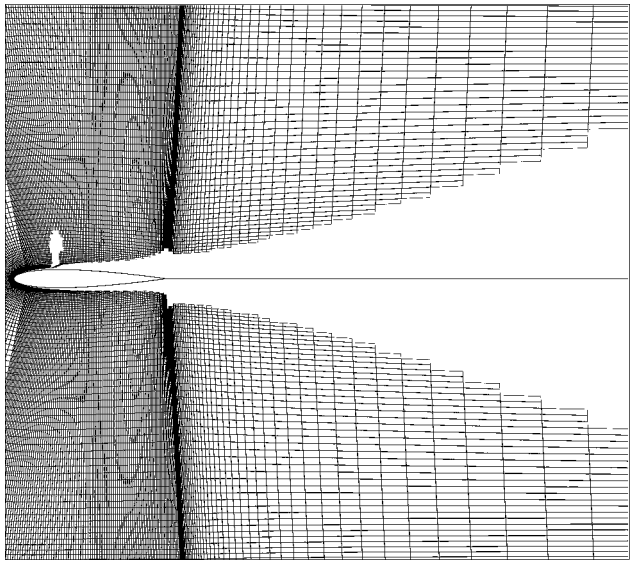

Fig. 9 NACA 0012, viscous test: viscous and shock wave regions selected in the fine-grid test, $M_\infty = 0.7$, $Re_\infty = 9 \times 10^6$, and $C_L = 0.424$.

been verified that the selected region, larger than the real wake, did not introduce any contribution to the spurious drag.

In Figs. 10–12, the drag polars computed on the medium, fine, and superfine grids are compared with the experimental data. In Figs. 10–12, the breakdown in viscous and wave drag is also suggested. Analysis of Fig. 10 shows that, even for a grid with only 128 cells around the airfoil, the identification of the spurious drag contribution (≈ 16 counts in this case) allows for a satisfactory prediction of $C_{D_v} + C_{D_w}$ (the total drag) over a wide range of lift coefficients. (The test at $C_L = 0.6$ is not reported because it is not fully converged on the medium level). For the fine level (Fig. 11), the detected spurious drag is ≈ 5 counts, and it reduces to ≈ 2 counts for the superfine level (Fig. 12). In both cases, the agreement of $C_{D_v} + C_{D_w}$ with the experiments is excellent. Figures 10–12 also show a satisfactory agreement for the viscous and wave drag contributions as computed on the different grids. The wave drag only appears at higher lift conditions, when the upper shock forms and, as expected, is strongly dependent on lift. The viscous drag dependence on lift is weaker; significant variations of C_{D_v} only appear when the shock/boundary-layer interaction becomes strong.

In Fig. 13, the wave drag polar computed on the fine grid level is compared with the result obtained for an inviscid simulation. As

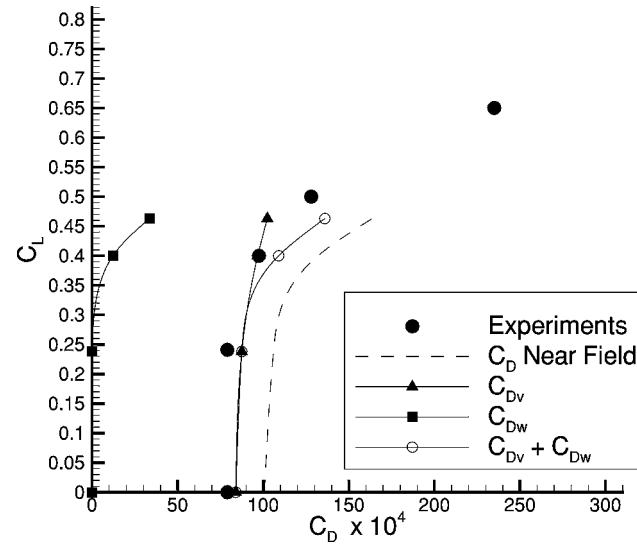

Fig. 10 NACA 0012, viscous test: comparison of the drag polars, medium-grid test, $M_\infty = 0.7$, and $Re_\infty = 9 \times 10^6$.

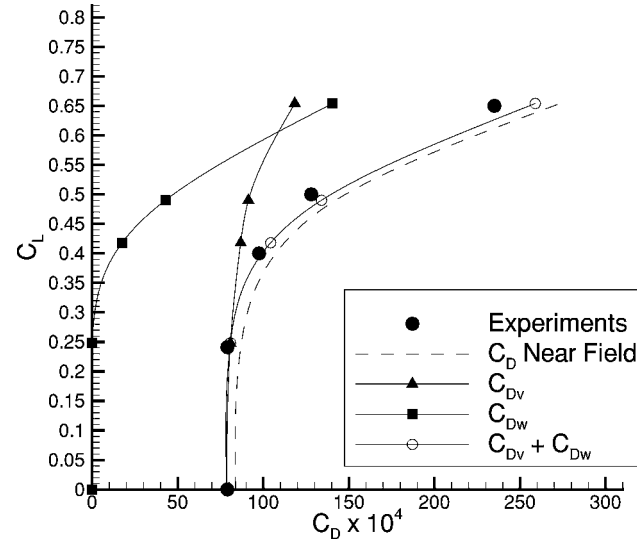

Fig. 11 NACA 0012, viscous test: comparison of the drag polars, fine-grid test, $M_\infty = 0.7$, and $Re_\infty = 9 \times 10^6$.

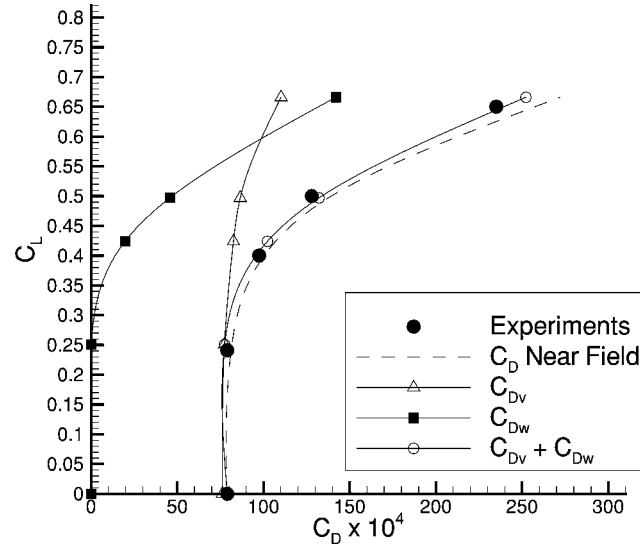

Fig. 12 NACA 0012, viscous test: comparison of the drag polars, superfine-grid test, $M_\infty = 0.7$, and $Re_\infty = 9 \times 10^6$.

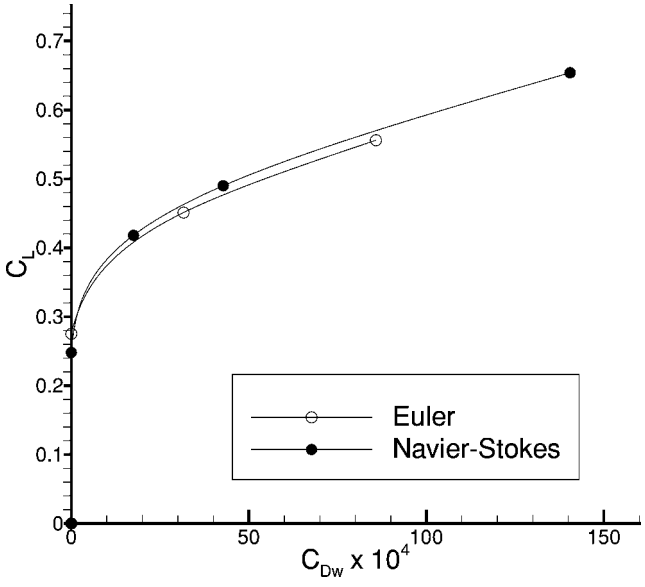

Fig. 13 NACA 0012, comparison of the wave drag polars computed for the viscous (fine grid) and inviscid (fine grid) test case, $M_\infty = 0.7$, and $Re_\infty = 9 \times 10^6$ (viscous test).

expected, the different shock location induced by the boundary-layer interaction decreases the wave drag in the viscous flow when compared with the inviscid result at fixed lift.

C. Accuracy of Results

Variations of 1 drag count have a significant impact on aircraft performance at transonic speeds[3]; however, a drag prediction within 1 drag count accuracy is still a big challenge even with use of experimental tools. It is further complicated when the data need to be extrapolated to real flight conditions.

If drag is computed by a numerical method, there are two main sources of uncertainties in the obtained results: 1) the accuracy of the computed flow field and 2) the accuracy of the the method adopted for the calculation of the drag of the given flowfield.

1. *Accuracy of Computed Flowfield*

This work is concentrated on the "extraction" of drag from a given numerical flowfield and is not concerned with the numerical method adopted for the computation of the flow itself. However, it is useful to look at some aspects related with the accuracy of the available flow solutions.

An example of the convergence histories of the numerical computation of the viscous flow is shown in Fig. 14 (average time derivative of density vs time iterations on the four grid levels). The final numerical residual is reduced at 10^{-6} times the initial residual. (In the inviscid test, it reached the zero of the floating point double precision computation.) The near-field lift and drag coefficients reached a steady value, and the flow solutions can be certainly considered fully converged on all grid levels.

Comparison of the pressure distributions obtained on the body by the different levels of refinement of the grid suggests that the results are converged as $h \to 0$ (Fig. 2 for the inviscid test and Fig. 5 for the viscous test), and the agreement with the experimental results is good in spite of the simple algebraic turbulence model, as already discussed. A more careful study to assess the convergence of the numerical solution for $h \to 0$ requires the analysis of the behavior with h of some norm of the numerical error (Richardson extrapolation), as suggested, for instance, in Ref. 18.

A similar procedure is proposed in Ref. 19; the global accuracy of the numerical solution is obtained by extrapolating the near-field drag to zero mesh size assuming $C_D(h) = c_0 + c_1 h + c_2 h^2$ with the coefficients of the parabola c_i computed by interpolating the results obtained on three different grid levels. The numerical algorithm adopted for the flow calculations is second-order accurate on

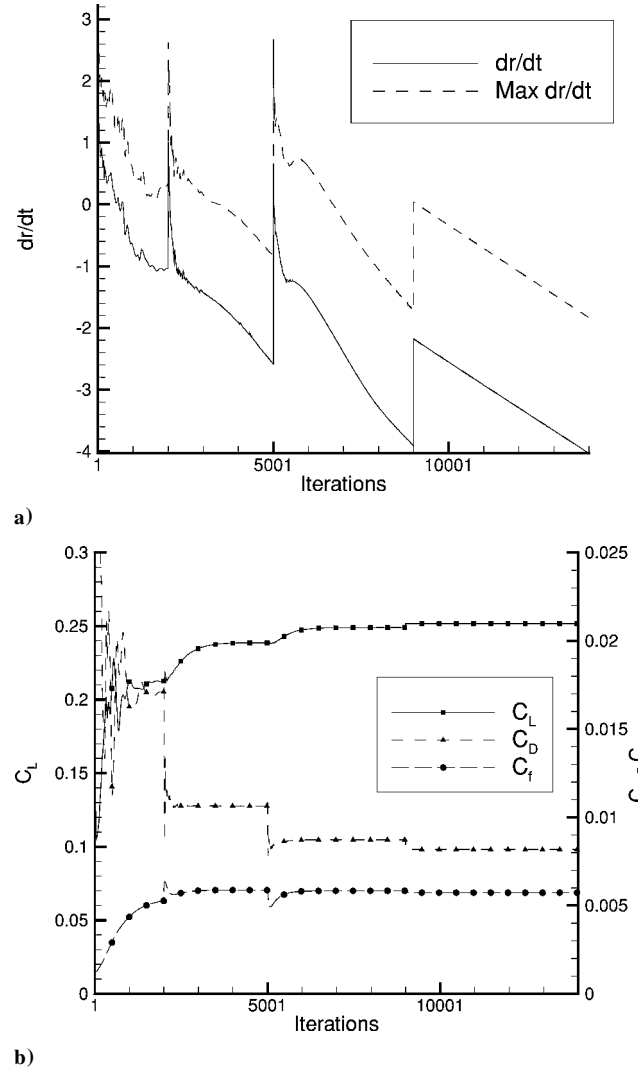

Fig. 14 NACA 0012, viscous test, convergence history: a) ——, average and – – –, maximum time derivative of density vs time iterations and b) force coefficients vs time iterations, near-field lift C_L, near-field drag C_D, and friction drag C_F, $M_\infty = 0.7$, $Re_\infty = 9 \times 10^6$, and $C_L = 0.254$.

Cartesian grids (except near shocks); nonetheless, it is well known that grid stretching and skewness introduce a first-order error contribution. Near-field C_D vs mesh size is plotted in Fig. 15 with $M_\infty = 0.7$, $Re_\infty = 9 \times 10^6$, and $C_L = 0$. The C_D computed on the superfine grid matches quite well the parabolic fitting of the coarser level values (Fig. 15, square symbols), confirming that the results are converging as $h \to 0$.

On the superfine grid, the computed near-field drag is 79 counts vs 84 counts for the fine grid; the extrapolated value at zero mesh is 76 counts. The experiment of Harris[16] provides 75 drag counts. Following the statistical analysis of McCroskey[20] of approximately 50 experiments on the NACA 0012 airfoil, in Ref. 17 for this flow condition, the range 73–83 drag counts is proposed based on six experiments quoted as best measurements. (Harris's measurement is among them.)

2. *Accuracy of Far-Field Drag Calculations*

The far-field drag formulas proposed here, based on a Taylor's series expansion, could be another source of error in the drag evaluation. However, the analysis of Table 1 (results referred to the $h = 2$ grid) shows that differences with respect to the exact drag expression (7) are smaller than 1 count if second-order entropy terms are taken into account.

Present far-field analysis suggests 76 counts with 2 counts of spurious drag detected on the superfine grid. (Note that it is coincident

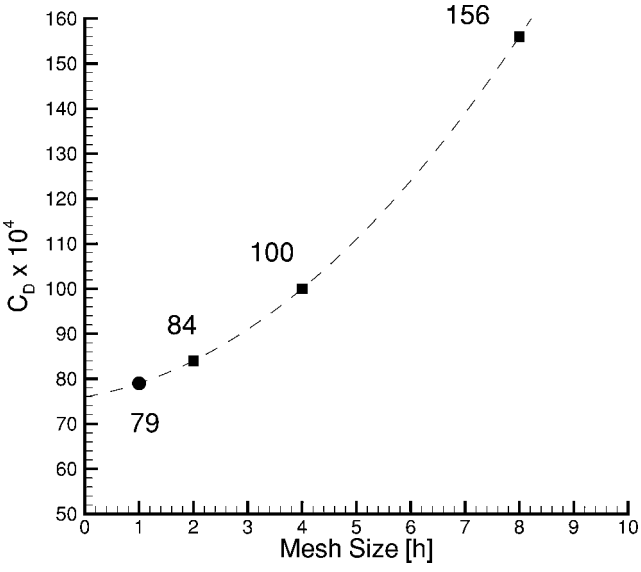

Fig. 15 NACA 0012, viscous test: near-field C_D vs mesh size, $M_\infty = 0.7$, $Re_\infty = 9 \times 10^6$, and $C_L = 0$.

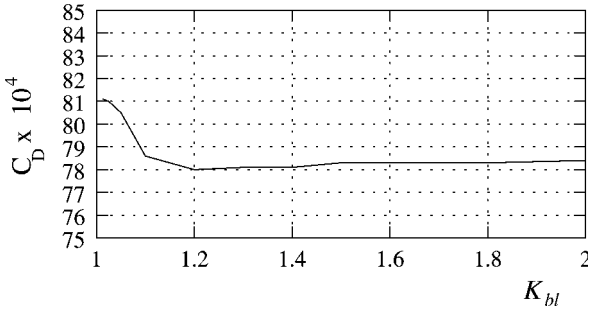

Fig. 16 NACA 0012, fine grid viscous test: viscous drag coefficient vs boundary-layer cutoff parameter, $M_\infty = 0.7$, $Re_\infty = 9 \times 10^6$, and $C_L = 0$.

with the zero mesh extrapolated value.) On the fine and medium grids, 79 and 84 drag counts have been computed.

The drag coefficient detected on the superfine grid is only 1 count lower than the C_D measured by Harris[16] and, at least in this case, is coincident with the near-field value extrapolated to zero mesh (Fig. 15).

To verify the sensitivity of the breakdown procedure to the input cutoff parameters, Fig. 16 shows the computed viscous drag vs the cutoff parameter K_{bl}. For $K_{\text{bl}} = 1$, the complete flow domain is selected; therefore, the computed value also contains the spurious contribution. When K_{bl} is increased, the spurious contribution is removed, and the computed drag quickly stabilizes. A choice of K_{bl} in the range (1.1, 2) provides variations in the computed C_D lower than 1 count.

Provided an accurate numerical flow solution, analysis of the present results suggests that the proposed far-field method allows for a drag estimation within 1 count accuracy, when compared with the results extrapolated to zero mesh size, if a mesh refinement, here defined as superfine, is adopted. On fine grids the error is ≈ 3 counts and on medium-sized grids ≈ 8 counts. The latter is the most representative of the mesh resolution feasible in engineering applications for complex three-dimensional configurations (current computing power available). This error is comparable with the uncertainties of the experimental results analyzed by McCroskey.[20]

VIII. Wing–Body, Viscous Flow

Some results obtained on a wing–body transonic configuration are presented. The freestream flow conditions are $M_\infty = 0.75$ and $Re_\infty = 4.3 \times 10^6$. Wind-tunnel experiments are presented in Ref. 21.

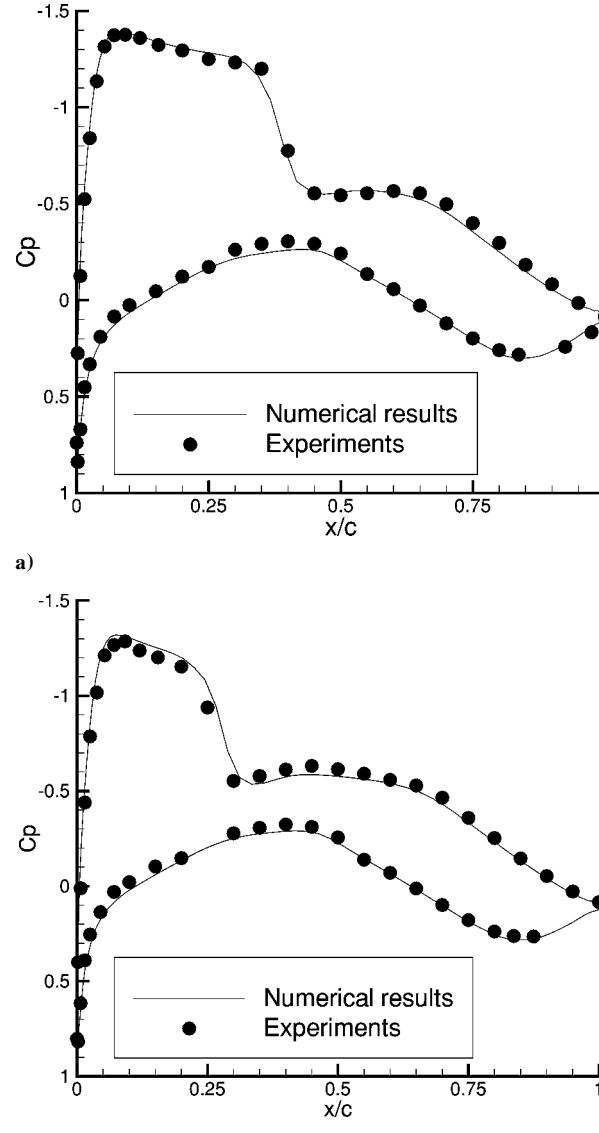

Fig. 17 Wing–body, viscous test, surface pressure distributions, $M_\infty = 0.75$, $Re_\infty = 4.3 \times 10^6$, and $C_L = 0.6$: a) $y/(b/2) = 0.62$ and b) $y/(b/2) = 0.87$.

This test is interesting because shows the feasibility of computing and decomposing the entropy drag in the case of complex three-dimensional flows. Furthermore, it illustrates that, in practical applications (block structured grids and skewness and stretching of the grid at block interfaces), the identification of the spurious drag contribution is even more important. The mesh used is a 41-block grid made up of 1,600,513 points on the finest level, built by The Netherlands National Aerospace Laboratory in the frame of a European research project.[22]

In Fig. 17, the computed pressure distributions are compared with the experiments for two wing sections and show excellent agreement. Nevertheless, inspection of the flow solutions reveals the presence of a large production of spurious drag in regions where discontinuities of the grid are unavoidable. An example is given in Fig. 18, where the isocurves of the local production rate of drag are plotted in a section near the wing leading edge. The local drag production rate for the j-grid cell is given by

$$\dot{d} = \frac{10{,}000}{1/2\rho_\infty V_\infty^2 S_{\text{ref}}} \int_{S_j} \boldsymbol{n} \cdot \rho g \boldsymbol{V} \, \mathrm{d}S_j \tag{25}$$

and represents the number of drag counts per unit volume locally produced in the flow domain. In Fig. 18, a similar plot obtained for

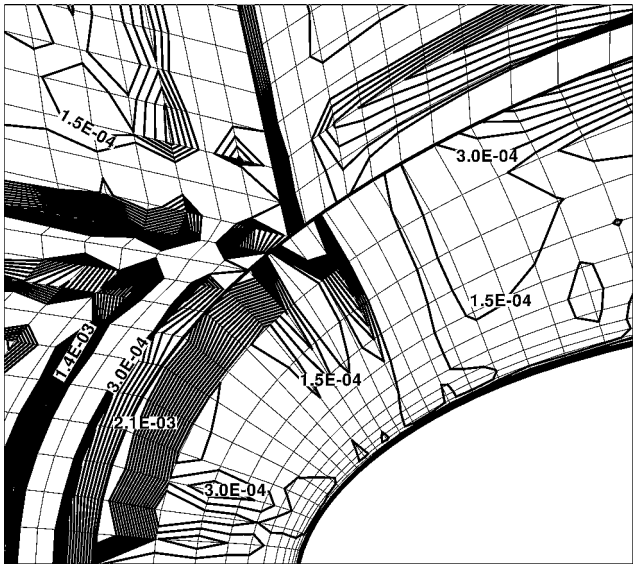

a)

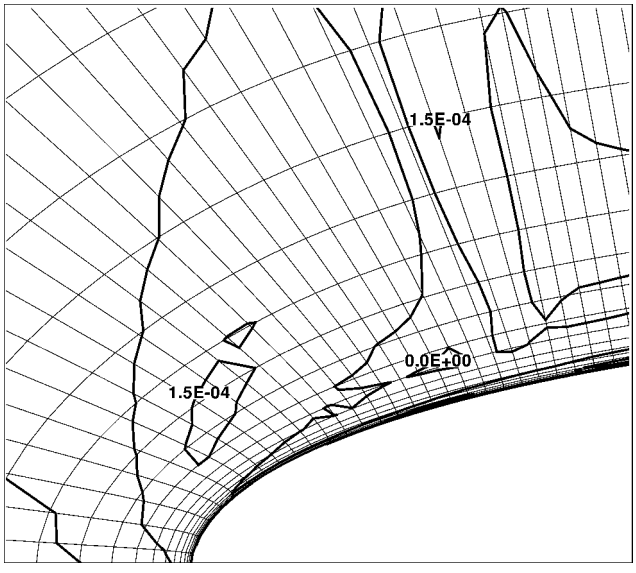

b)

Fig. 18 Local drag production rate $\dot{d}$ close to the wing leading edge: a) wing–body viscous test, $M_\infty = 0.75$, $Re_\infty = 4.3 \times 10^6$, $C_L = 0.5$, section $y/(b/2) = 0.5$ and b) NACA 0012 viscous test, $M_\infty = 0.7$, $Re_\infty = 9 \times 10^6$, and $C_L = 0.5$.

the NACA 0012 viscous test is presented. For the wing–body test (fine grid) $\dot{d}$ is an order of magnitude larger outside the boundary layer, when compared with the NACA 0012 test (medium grid).

This problem is also highlighted when near-field drag coefficients computed on the successively refined grids are compared. The obtained values for the near-field C_D are 592, 363, and 304 drag counts on the coarse, medium, and fine grids, respectively. Although the drag is converging as $h \to 0$, the difference between the C_D on the finest level and the value extrapolated to zero mesh is still large (≈ 30 counts, a value close to the $C_{D_{sp}}$ predicted by present method).

Finally, in Fig. 19, the breakdown of the entropy drag into viscous and wave components is presented. In this case, the far-field drag cannot be compared with the near-field value because the present method does not account for the vortex drag. However, in Fig. 19, a vortex drag C_{D_i} estimation by a different method is also plotted. C_{D_i} has been computed by Maskell's formula, in which the drag due to lift is related to a vorticity integral in the Trefftz plane (see Refs. 7, 8, and 12).

The experimental polar curve cannot be considered as a reference for the validation of the present breakdown of the total drag. This

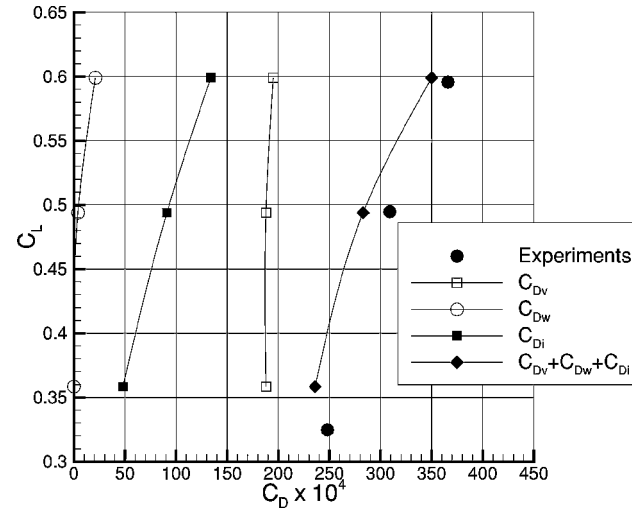

Fig. 19 Wing–body viscous test: viscous, wave, and induced-drag polars, $M_\infty = 0.75$, and $Re_\infty = 4.3 \times 10^6$.

is because the experiments on the half model of the clean wing–body configuration were devoted to the computation of the engine installation drag, and therefore, a scatter in the total drag values is expected. Furthermore, a slight variation of the numerical C_{D_i} with the position of the Trefftz plane has been verified, indicating a small range of uncertainty for the total computed drag ($C_{D_v} + C_{D_w} + C_{D_i}$).

IX. Conclusions

A far-field method for accurate calculation of the entropy drag has been proposed that relies on a given numerical solution of the RANS equations. The method allows for the decomposition of the drag in its viscous and wave contributions once the boundary-layer and the shock wave regions are identified in the numerical flow domain. For this purpose, a robust algorithm has been introduced for the selection of the boundary-layer/wake and shock wave zones.

The method has been tested by determining the polar curves for a transonic airfoil flow with grids of different mesh size. It has been shown that Oswatitsch's classical formula is not accurate in viscous flows, but a second-order correction term, here proposed, is required.

The far-field drag calculation is equivalent to the near-field analysis, with both methods converging as mesh size becomes infinitely small. The agreement with experimental results is excellent as far as the numerical solution is accurate. Moreover, once the the boundary-layer and the shock wave regions are selected, by present method, it is possible to compute and remove a substantial part of the spurious drag introduced by the discretization error of the flow solver. As consequence, the corrected drag is only weakly dependent on grid size, implying accurate drag calculations even on medium sized grids.

The algorithm of region selection enabled a definition of viscous and wave drag for the numerical solutions of the Navier–Stokes equations, which allowed the breakdown of the entropy drag, useful information for the aircraft designer.

The algorithm has also been tested by studying a wing–body configuration in transonic flow, demonstrating the capability to analyze more complex and realistic aircraft configurations, although for the case of the computation of the total drag, the calculation of the vortex drag by a different method is also required. The three-dimensional test also revealed that, in the case of a multiblock structured grid with skewness and stretching at block interfaces, the contribution of the spurious drag is even more important.

Acknowledgments

The present work has been partially developed in the frame of the Aircraft Drag and Thrust Analysis Research Project funded by the European Commission (Contract BPR-C197-470). The authors are grateful to M. Laban and S. Spekreijse of the National Aerospace Laboratory (The Netherlands) for their help and their support in providing the code for the induced drag computation. The authors

also thank D. Destarac (ONERA), C. P. van Dam (University of California, Davies) and A. Pozzi (University of Naples) for fruitful discussions.

References

[1]Slooff, J. W., "Computational Drag Analysis and Minimization; Mission Impossible?," *Proceedings of the Aircraft Drag Prediction and Minimization Symposium*, R-723, AGARD, 1986, Addendum 1.

[2]van der Vooren, J., and Slooff, J. W., "CFD-Based Drag Prediction; State of the Art, Theory, Prospects," Lectures Notes, AIAA Professional Studies Series, Course on Drag-Prediction and Measurement, Dutch Aerospace Lab., NLR TP 90247, 1990.

[3]van Dam, C. P., "Recent Experience with Different Methods of Drag Prediction," *Progress in Aerospace Sciences*, Vol. 35, 1999, pp. 751–798.

[4]Prandtl, L., and Tietjens, O. G., *Applied Hydro- and Aeromechanics*, Dover, New York, 1934, p. 125.

[5]Oswatitsch, K., *Gas Dynamics*, Academic Press, New York, 1956, pp. 177–210.

[6]Lock, R. C., "The Prediction of the Drag of Aerofoils and Wings at High Subsonic Speeds," *Aeronautical Journal*, Vol. 90, No. 896, 1986, pp. 207–226.

[7]Giles, M. B., and Cummings, R. M., "Wake Integration for Three-Dimensional Flowfield Computations: Theoretical Development," *Journal of Aircraft*, Vol. 36, No. 2, 1999, pp. 357–365.

[8]Hunt, D. L., Cummings, R. M., and Giles, M. B., "Wake Integration for Three-Dimensional Flowfield Computations: Applications," *Journal of Aircraft*, Vol. 36, No. 2, 1999, pp. 366–373.

[9]Chao, D. D., and van Dam, C. P., "Airfoil Drag and Decomposition," *Journal of Aircraft*, Vol. 36, No. 4, 1999, pp. 675–681.

[10]Schmitt, V., and Destarac, D., "Recent Progress in Drag Prediction and Reduction for Civil Transport Aircraft at ONERA," AIAA Paper 98-0127, Jan. 1998.

[11]Masson, C., Veilleux, C., and Paraschivoiu, I., "Airfoil Wave-Drag Prediction Using Euler Solutions of Transonic Flows," *Journal of Aircraft*, Vol. 35, No. 5, 1998, pp. 748–753.

[12]van Dam, C. P., Nikfetrat, K., Wong, K., and Vijgen, P. M. H. W., "Drag Prediction at Subsonic and Transonic Speeds Using Euler Methods," *Journal of Aircraft*, Vol. 32, No. 4, 1995, pp. 839–845.

[13]Martinelli, L., "Calculations of Viscous Flows with a Multigrid Method," Ph.D. Dissertation, Mechanical and Aerospace Engineering Dept., Princeton Univ., Princeton, NJ, Oct. 1987.

[14]Baldwin, B. S., and Lomax, H., "Thin Layer Approximation and Algebraic Model for Separated Turbulent Flows," AIAA Paper 78-257, Jan. 1978.

[15]Spalart, P. S., and Allmaras, S. R., "A One Equation Turbulence Model for Aerodynamics Flows," AIAA Paper 92-0439, Jan. 1992.

[16]Harris, C. D., "Two Dimensional Aerodynamic Characteristics of the NACA 0012 Airfoil in the Langley 8-Foot Transonic Pressure Tunnel," NASA TM 81927, April 1981.

[17]Holst, T. L., "Computational Fluid Dynamics Drag Prediction—Results from the Viscous Transonic Airfoil Workshop," Rept. AR-256, AGARD, June 1989.

[18]Roache, P. J., *Verification and Validation in Computational Science and Engineering*, Hermose, Albuquerque, NM, 1998.

[19]Oskam, B., and Slooff, J. W., "Recent Advances in Computational Aerodynamics at NLR," AIAA Paper 98-0138, Jan. 1998.

[20]McCroskey, W. J., "A Critical Assessment of Wind Tunnel Test Results for the NACA 0012 Airfoil," AGARD Fluid Dynamics Panel Symposium on Aerodynamic Data Accuracy and Quality: Requirements and Capabilities in Wind Tunnel Testing, AGARD, Paper 1, 1987.

[21]"ONERA Tests on the ALVAST Half Model Equipped with TPS6402, VHBR2 and CRUF2 Powered Nacelles in Test Section no 1-40 m^2 of SIMA, Wind Tunnel Test Report," ONERA, TR 2/8055 DSMA/Y, Feb. 1999.

[22]Laban, M., "Aircraft Drag and Thrust Analysis (AIRDATA) Project Overview and Key Results," *Proceedings of the Workshop on EU-Research on Aerodynamic Engine/Aircraft Integration for Transport Aircraft*, DLR, German Aerospace Research Center, 2000, pp. 9–1, 9–15.

P. R. Bandyopadhyay
Associate Editor